Available online at www.sciencedirect.com
ScienceDirect
Trans. Nonferrous Met. Soc. China 35(2025) 4084−4100
Transactions of Nonferrous Metals Society of China
www.tnmsc.cn

Microstructure and mechanical properties of TIG and LBW welded Mg−8Li−3Al−2Zn−0.5Y alloy

Jia-wei LU[1], Hong-jie LIU[1], Lian-mei WU[2], Jia-xin YU[1], Yu-chuan HUANG[1], Jia-wei SUN[1], Guo-hua WU[1], Wen-xia HU[2], Fei LI[2], Jun-feng LI[3], Wen-cai LIU[1]

1. National Engineering Research Center of Light Alloy Net Forming and State Key Laboratory of Metal Matrix Composite, School of Materials Science and Engineering, Shanghai Jiao Tong University, Shanghai 200240, China;
2. Beijing Institute of Electronic System Engineering, Beijing 100854, China;
3. Shanghai Cloud-Manu 3D Technology Co., Ltd., Shanghai 201306, China

Received 21 April 2024; accepted 19 May 2025

Abstract: Tungsten inert gas (TIG) welding and laser beam welding (LBW) were employed on as-cast and as-forged Mg−8Li−3Al−2Zn−0.5Y (LAZ832-0.5Y) alloys to investigate their weldability. The microstructure and mechanical properties of solid solution treated samples were investigated for the purpose of further strength improvement, which were treated at 350 °C for 4 h. The ultimate tensile strength (UTS) and yield strength (YS) of the optimal TIG as-cast alloy welding joint were 159 and 122 MPa, which were obtained under the welding current of 80 A, and were lower than the UTS (184 MPa) and YS (146 MPa) of the optimal LBW as-forged welding joint under the power of 2.1 kW/2.0 kW double-side welding. After the solid solution treatment, on the one hand, the growth of α-Mg grains in the fusion zone (FZ), heat affected zone (HAZ) and base metal (BM) of both the TIG and LBW welding joints was insignificant. On the other hand, the larger Al_2Y phases were still present, while the much smaller white AlLi particles were dissolved into the matrix, leading to the solid solution strengthening of the welding joints. As a result, the UTS and YS of the TIG welding joint respectively increased to 216 and 188 MPa after solid solution treatment, and those of the LBW welding joint only increased to 211 and 160 MPa, respectively.

Key words: Mg−Li alloy; tungsten inert gas welding; laser beam welding; microstructure; mechanical properties; heat treatment

1 Introduction

Magnesium−lithium (Mg−Li) alloys have recently attracted much attention due to their lower densities (1.35−1.65 g/cm^3) among all Mg alloys, and shown great potential for aerospace, military and electronic products applications [1−5]. A novel Mg−8Li−3Al−2Zn−0.5Y (denoted as LAZ832-0.5Y) developed by ZHAO et al [6,7] and JI et al [8], with a duplex microstructure consisting of α-Mg and β-Li, exhibited better comprehensive mechanical properties than conventional Mg−Li alloys [9−12]. It is critical to investigate the weldability of Mg−Li alloys, as a result of the increasing welding demand of Mg−Li alloys due to the increasing applications in the field of aerospace industry and electronic 3C products [2,3]. However, only limited research has focused on the weldability of Mg−Li alloys [13−16], especially on the conventional welding approaches. Besides, the welding process of Mg−Li alloys is challenging as the Mg and Li elements are easily oxidized and burned during the welding process [17,18]. Thus, the welding process of Mg−Li alloys

Corresponding author: Wen-cai LIU, Tel: +86-21-54742630, Fax: +86-21-34202794, E-mail: liuwc@sjtu.edu.cn
https://doi.org/10.1016/S1003-6326(25)66931-7

is worth investigating.

So far, the most adopted welding techniques for Mg−Li alloys include friction stir processing (FSP), laser beam welding (LBW), and tungsten inert gas welding (TIG). FSP can effectively refine the grains and further improve the mechanical properties of the alloys [14,15,19]. On the other hand, the FSP is challenging because the disk-shaped workpiece and thin-walled pipe fittings are hard to clamp [13]. LBW of Mg−Li alloys may effectively solve the grain coarsening in the fusion zone due to its high energy density and low heat input [20,21]. During the TIG process, the protective gas is continuously sprayed from the nozzle of the welding torch, protecting the molten pool and the adjacent heat affected zone and resulting in welding seams of high quality [13,22].

TIG welding on the Mg−14Li−1Al (LA141) plate using the welding wire with the diameter of 2 mm was conducted by WU et al [23]. The ultimate tensile strength (UTS) of the welded LA141 plate reached 153 MPa, which accounted for 95% that of the base metal, while the elongation to fracture remained approximately 8%. LIU et al [22] performed TIG welding on an ultra-light Mg−10.36Li−2.7Al−0.91Zn−0.81Ce plate with a thickness of 2 mm, using a welding current of 80 A. The tensile strength of the welded joint was only 84% that of the parent metal. These results suggested that the weldability of the Mg−Li alloys using TIG welding may be poor and needs to be further investigated. In addition, better understanding will be achieved by more systematic work in the future. ZHANG et al [20] carried out the LBW of the Mg−10Li−3Al−3Zn alloy, with a laser power of 2.8 kW and a welding speed of 4 m/min. The UTS of the welding joint was 166.8 MPa, which was about the same value of the base metal (167.7 MPa). In addition, the microstructure in the fusion zone is much finer than that of the base metal. This investigation indicated that LBW may be an effective welding method for Mg−Li alloys. However, similar to the TIG welding [24,25], more systematic work is still needed for further understanding of the LBW approach.

The aim of the present study is to provide systematic investigations on the TIG and LBW welding processes of the LAZ832-0.5Y alloy. The welding joints of the LAZ832-0.5Y alloy using TIG and LBW with various parameters were fabricated and their microstructure and mechanical properties were then characterized. In addition, solid solution treatments were conducted on the welding joints to further improve the mechanical properties.

2 Experimental

2.1 Preparation of LAZ832-0.5Y wires

The as-cast LAZ832-0.5Y alloy was prepared by smelting commercially pure (CP, 99.9 wt.%) Mg, Li, Al, Zn, and Mg−20Y (wt.%) master alloy in a vacuum induction melting furnace under the protection of argon atmosphere. The detailed information on casting process can be found in Ref. [6]. The billets with dimensions of d85 mm × 100 mm were machined from the as-cast ingots and held at 275 °C for 2 h prior to extrusion. The wires with a diameter of 1.2 mm were obtained by extrusion at 260 °C with an extrusion ratio of roughly 5000:1. The chemical composition of the wires was analyzed by inductively coupled plasma-atomic emission spectroscopy (ICP-AES, PerkinElmer Plasma−400), as shown in Table 1. The wires were used for TIG welding in the present study. The microstructure of the wires can be found in Ref. [13].

Table 1 Chemical composition of as-cast ingot (wt.%)

Li	Al	Zn	Y	Mg
8.6	3.4	1.6	0.4	Bal.

2.2 TIG and LBW welding processes

To provide more comparison bases, the base alloys in two different states were selected. The TIG welding was carried out on the as-cast LAZ832-0.5Y plates whilst the LBW welding was performed on the as-forged LAZ832-0.5Y plates. The as-forged LAZ832-0.5Y plate was produced by the forging process of the as-cast LAZ832-0.5Y alloy. The as-cast ingot was firstly homogenized at 275 °C for 4 h and then forged at 275 °C.

For TIG welding, the as-cast LAZ832-0.5Y welding plates with dimensions of 80 mm × 40 mm × 6 mm were cut out, and the welding bevels were machined on the edges of the welding plates. Prior to welding, the surfaces of the plates and the filler wires were cleaned with grinding sandpaper and degreased with acetone to remove the potential surface attachments. To ensure the

consistency of the welding seam, the plates were fixed on the welding platform. The spacing between the two plates was consistently less than 0.5 mm and the height difference of the two plates was less than 1 mm. The plates were welded using various welding currents, as shown in Table 2, where 100-d condition means that the plates were welded using double wires under a current of 100 A, and different welding currents were employed to select the suitable processing parameters.

Table 2 Parameters of TIG welding process

Experimental No.	Welding current/A	Filler wire diameter/mm	Argon gas flow rate/(L·min^{-1})	Welding speed/(m·min^{-1})
1	60	1.2	10	1.14
2	80	1.2	10	1.14
3	90	1.2	10	1.14
4	100	1.2	10	1.14
5	100-d	1.2	10	1.14
6	120	1.2	10	1.14

For LBW welding, the welding plates with a thickness of 5 mm were cut from the as-forged LAZ832-0.5Y billet. Compared with the TIG welding process, laser beam was adopted as the heating source in the LBW welding and no filler wires were needed. The plates were welded using various laser powers for comparison, as can be seen in Table 3. In Table 3, the laser power of 2.3 kW was adopted in both the conditions c and e, but the back shielding (BS) was used in condition c. In condition h, 2.1/2.0 means the plates were welded using double-laser beams on both sides simultaneously, with powers of 2.1 and 2.0 kW, respectively. Moreover, the laser power was controlled during the welding process.

Table 3 Parameters of LBW welding process

Experimental No.	Laser power/kW	Argon gas flow rate/(L·min^{-1})	Welding speed/(m·min^{-1})
a	2.7	10	1.8
b	2.15	10	1.8
c	2.3 (BS)	10	1.8
d	1.7	10	1.8
e	2.3	10	1.8
f	2.5	10	1.8
g	3.0	10	1.8
h	2.1/2.0	10	1.8

2.3 Solid solution treatment

In order to optimize the microstructure and mechanical properties of the welding joints, the samples were kept at 350 °C for 4 h [8] under the protection of SO_2 atmosphere, followed by water quenching. The samples after solid solution treatment were denoted as as-quenched samples hereafter.

2.4 Characterization

The cross-section of the welded plates was observed by an optical microscope (OM; Zeiss Axio Observer A1) and a scanning electron microscope (SEM; Phenom XL) equipped with an energy-dispersive spectroscope (EDS).

The Vickers hardness (HV) measurements were carried out on a Vickers hardness tester (XHVT 10Z) using a load of 49 N and a dwelling time of 15 s. Rectangular tensile specimens across the welding seam with a gauge length of 15 mm were cut from the welding joints and the tensile tests were conducted using a universal tensile tester (Zwick/Roell Z020) at a nominal strain rate of 0.001 s^{-1}. Each test condition was repeated at least three times for repeatability and accuracy.

3 Results and discussion

3.1 Microstructure and mechanical properties of TIG welding joints

The microstructure of the as-cast LAZ832-0.5Y alloy was observed as the TIG welding was performed on the as-cast plates. As can be seen in Fig. 1(a), most of the white α-Mg grains were equiaxed while only a small fraction showed bar-shaped or needle-like morphology. This observation is consistent with results by WANG et al [26]. Without the addition of Y element, the α-Mg phase exhibited the long needle-like shape. With increasing Y content, the α-Mg phase became more and more globular while the size of it decreased firstly and then increased. In the case of present study, ICP results (Table 1) showed that the Y content was 0.4 wt.%. As a result, most of the α-Mg grains were equiaxed. As can be seen in Figs. 1(c, d), the larger faceted phase was identified

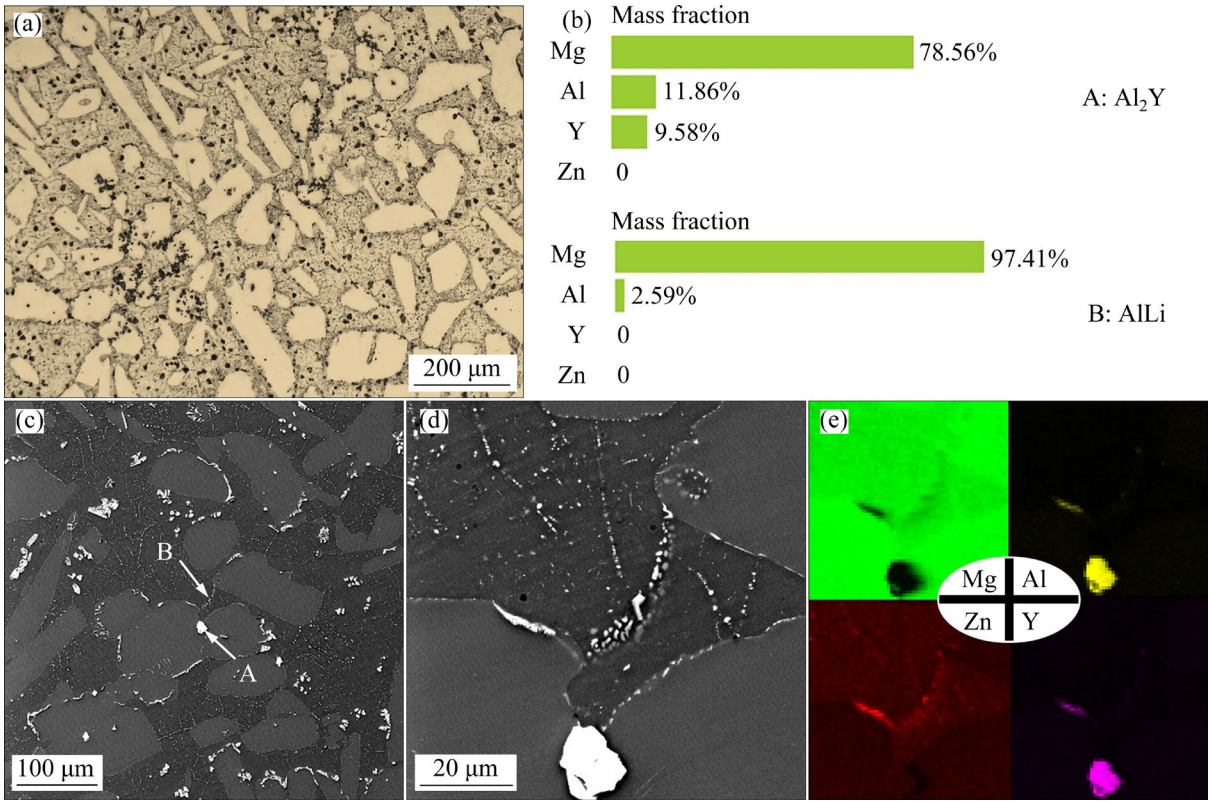

Fig. 1 Microstructures of as-cast LAZ832-0.5Y alloy: (a) OM image; (b) EDS point scan results in (c); (c) SEM image; (d) Magnified SEM image of (c); (e) EDS area scan results of (d)

to be the Al_2Y phase, while the much smaller white particles in Fig. 1(c) may be the AlLi phase [27]. The discrepancy between the as-measured Y content (0.4 wt.%) and the desired Y content (1 wt.%) can be explained by the formation of the Al_2Y phase.

Figure 2 shows the microstructures of the fusion zone (FZ), heat affected zone (HAZ) and base metal (BM) of TIG welding joints at various welding currents. The microstructure in the FZ was much finer than those in the HAZ and BM under all circumstances. Clearly, this significant grain-refinement phenomenon was caused by the fusion and subsequent fast cooling process in this region. Compared with the BM, the α-Mg phase was in the form of needle-like morphology, rather than the globular shapes. In addition, it is interesting to note that there were more needle-like α-Mg grains in the HAZ and the globular α-Mg grains were smaller than those in the BM regions. According to the Mg−Li binary phase diagram [28,29], when the temperature exceeds 591 °C, the α-Mg phase melted before the β-Li phase did. During the welding process, the temperature in the HAZ may have exceeded 591 °C due to the heat input in FZ and the α-Mg phase in this region experienced partial remelting and fast cooling. As a result, more needle-like α-Mg grains appeared due to fast cooling and the globular α-Mg grains were smaller due to the remelting. On the other hand, the needle-like α-Mg phase got coarser and coarser as the welding current increased from 60 to 120 A, due to increasing heat input. The microstructure of the 100-d A sample was comparable to that of 100 A sample. The temperature rise in 100-d A sample was lower than that in 100 A sample, because double wires were used under the 100-d A condition.

The SEM images in Fig. 3 are consistent with the OM images. The α-Mg, β-Li phases, Al_2Y and AlLi particles can be observed in the top area. In the FZ, both Al_2Y and AlLi phases can be seen clearly. Compared with the as-cast alloy (BM), Al_2Y and AlLi phases were finer and more homogeneously distributed across the whole material. In the HAZ, AlLi particles were dissolved in the matrix while the Al_2Y particles were still present.

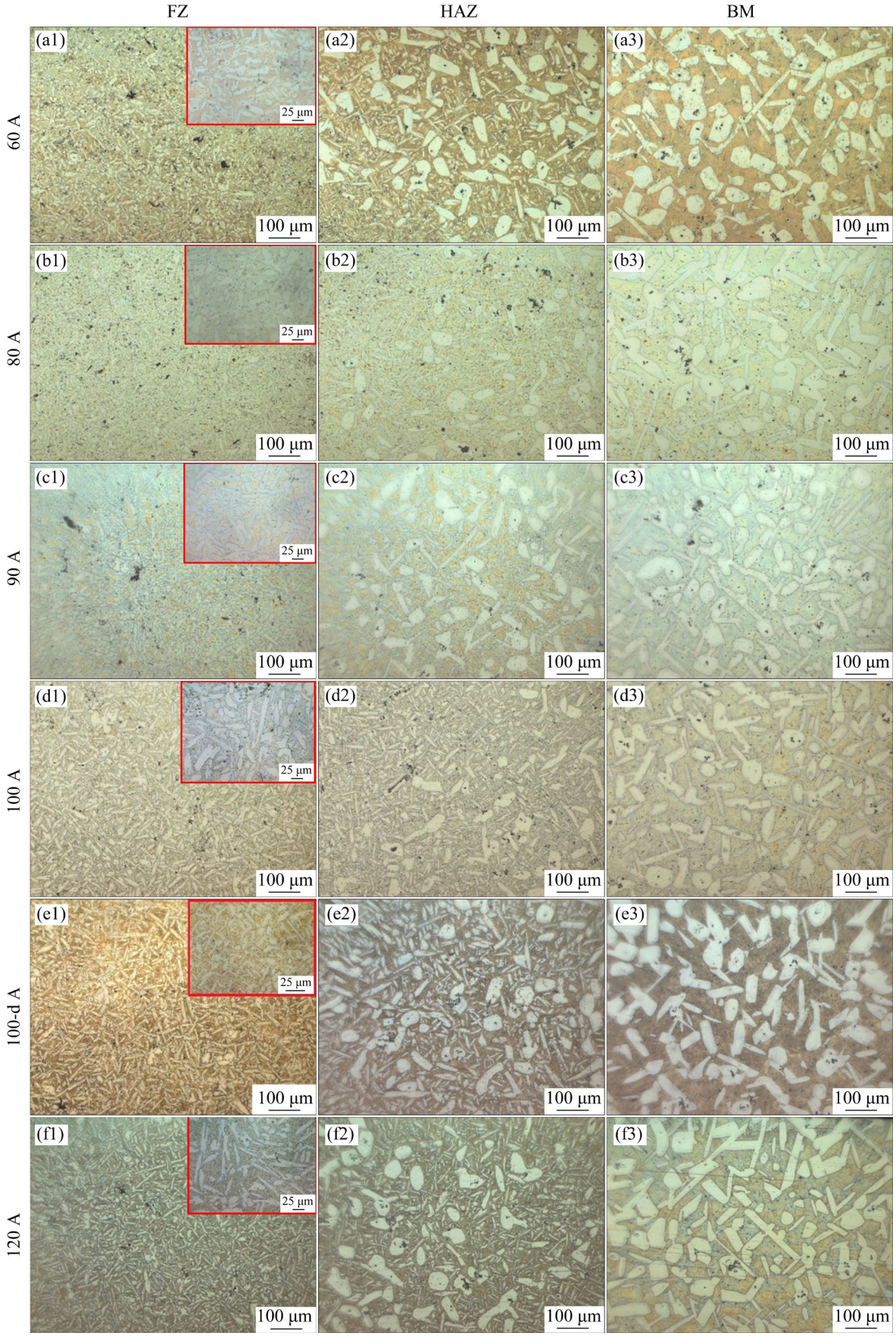

Fig. 2 OM images of FZ, HAZ and BM of TIG welding joints at various welding currents

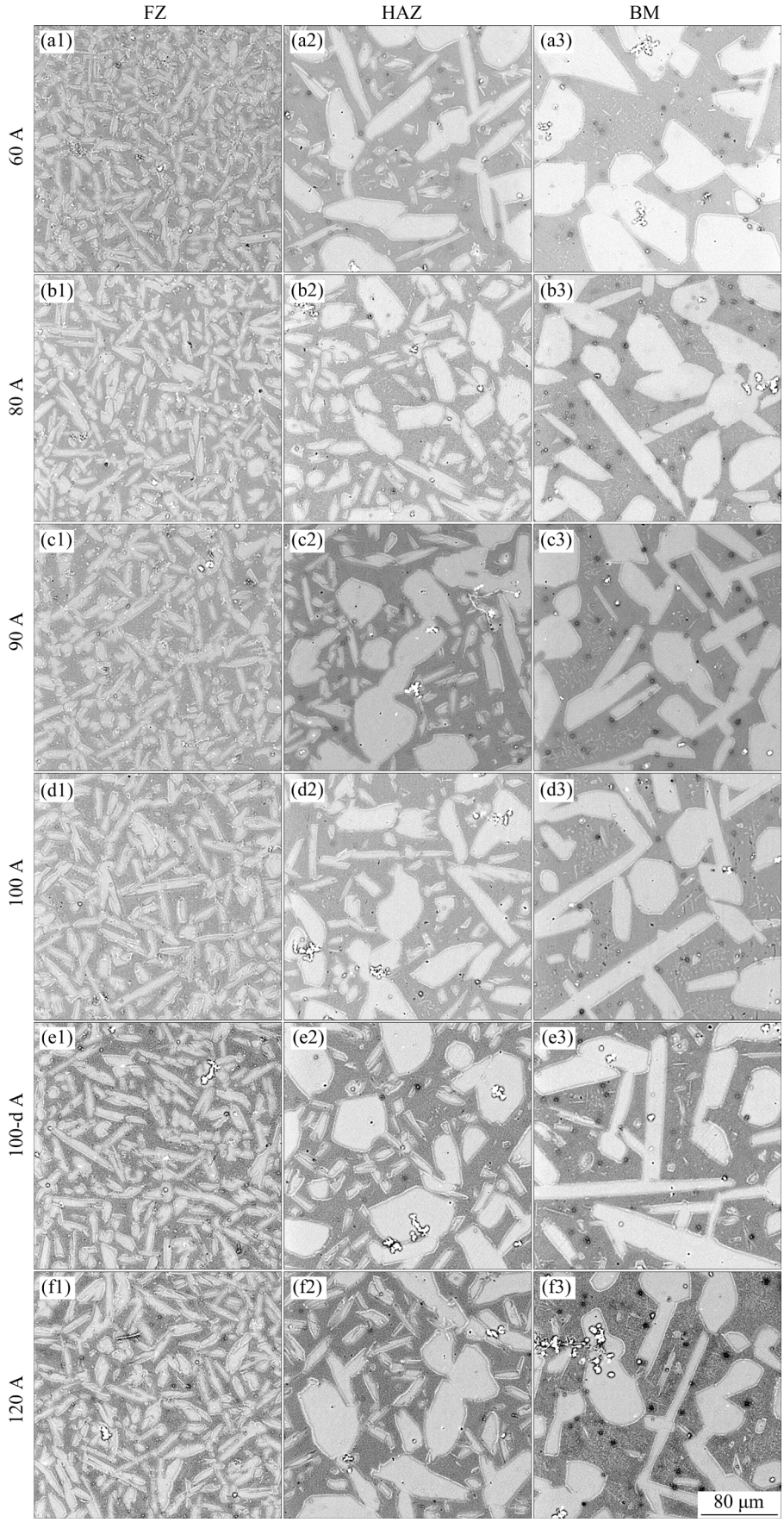

Fig. 3 SEM images of FZ, HAZ and BM of TIG welding joints at various welding currents

As shown in Fig. 4(a), Vickers hardnesses of the welding joints under various welding currents in both FZ and HAZ were higher than that of the BM (HV 51.38, indicated by the cyan horizontal line in Fig. 4(a)). No obvious differences in the hardness values can be seen, given the fluctuations in hardness measurements. The hardness values of the welding joint at a current of 120 A was consistently lower than those at currents of 60, 80, 90 and 100 A. As shown in Fig. 4(b), the ultimate tensile strength (UTS) and yield strength (YS) of all the welded joints were higher than those of the BM. In contrast, the elongation to fracture (EL) firstly decreased and then increased with increasing welding current, according to Fig. 4(c). The increase of UTS and YS may be related to the finer microstructures in FZ and HAZ shown in Fig. 2. In summary, the welded joint at a current of 80 A exhibited the optimal combination of mechanical properties: UTS of 159 MPa, YS of 122 MPa, and EL of 23%, exceeding the properties the as-cast alloy.

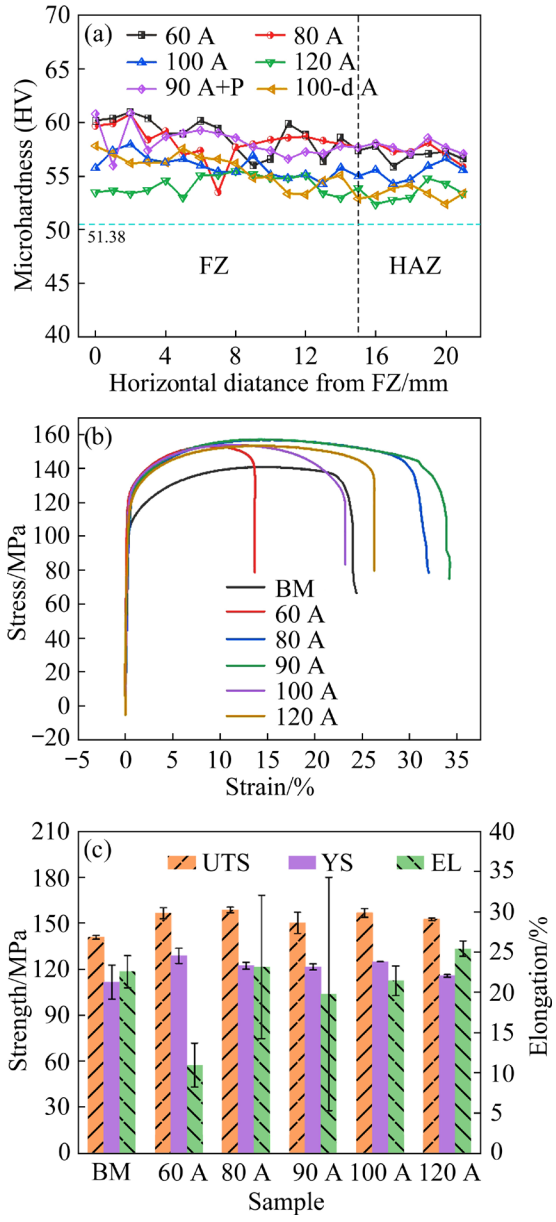

Fig. 4 Microhardness (a), tensile curves (b), and ultimate tensile strength (UTS), yield strength (YS) and elongation to fracture (EL) (c) of TIG welding joints at different welding currents (Vickers hardness of as-cast alloy is indicated by cyan horizontal line in (a))

3.2 Microstructure and mechanical properties of LBW welding joints

The α-Mg grains in the as-forged alloy were elongated along the horizontal direction, as can be seen in Fig. 5(a). In Fig. 5(d), the β-Li seemed to recrystallize after forging. Similar to the as-cast material, the Al_2Y and AlLi particles can still be distinguished easily by their morphologies in Fig. 5(d) and/or EDS results in Fig. 5(b).

Unlike the microstructure of the TIG welding joints, the boundaries between the FZ and HAZ in LBW welding joints were apparent (Fig. 6). This phenomenon may be due to the higher energy density of LBW technology. With the laser beam of much higher energy density, the fusion depth of LBW welding joints was much larger than that of TIG welding joint whilst the fusion width of the former was much smaller than that of the latter, leading to a distinct boundary between the FZ and HAZ. What was similar to the TIG welding joints was that the microstructure in FZ is much finer than that in the HAZ and BM. The microstructure in the FZ was too fine to be discerned so the effect of the laser power on the microstructure in the FZ was discussed based upon the SEM images. It is worthy to mention that the microstructure of the 2.3 kW BS welding seemed to consist of finer α-Mg phase than that of the 2.3 kW welding. However, the Vicker's hardness of the 2.3 kW welding was higher.

The SEM images of the FZ, HAZ-solution and HAZ-aging are shown in Fig. 7. There were plenty of Al_2Y and AlLi particles in the FZ. In contrast, the AlLi particles in the HAZ near the FZ disappeared and only the Al_2Y phase was present. In the HAZ away from the FZ, even more AlLi particles than those in the base metal appeared. The reason is that the heat input in the HAZ near FZ was high so that the AlLi particles were dissolved. On the contrary, the heat input in the HAZ away from FZ was low

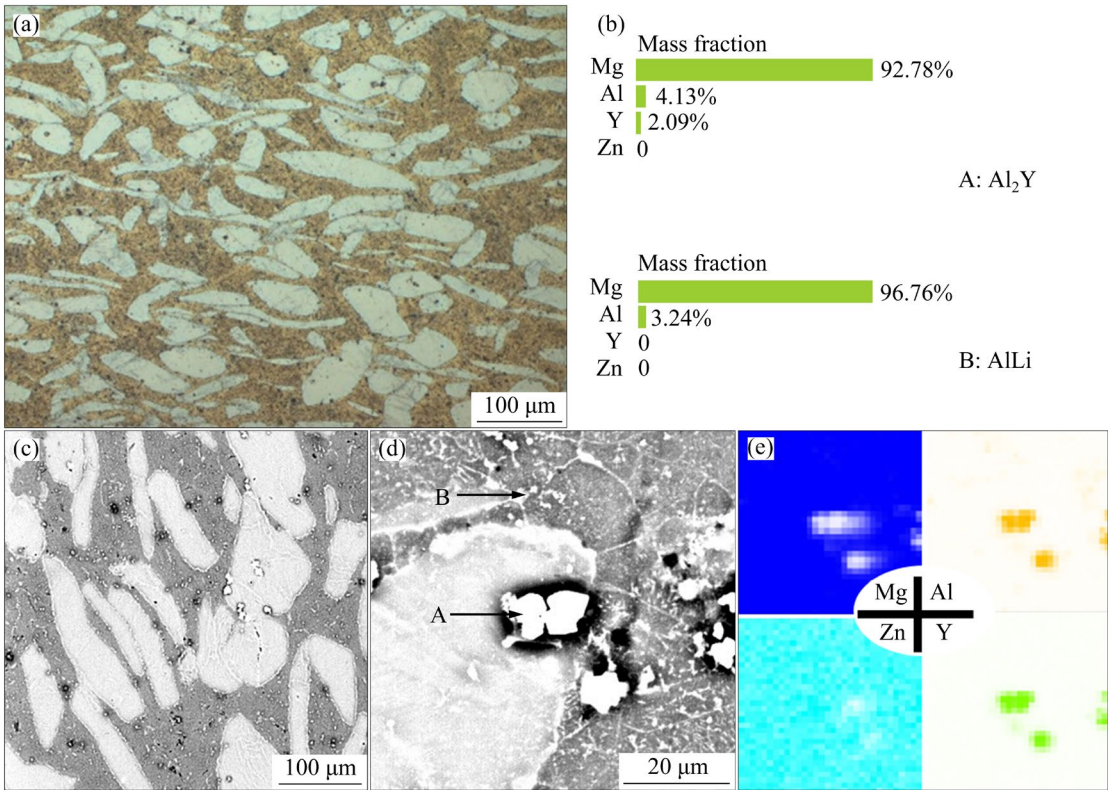

Fig. 5 Microstructures of as-forged LAZ832-0.5Y alloy: (a) OM image; (b) EDS point scan results in (d); (c) SEM image; (d) Magnified SEM image of (c); (e) EDS area scan results of (d)

enough to trigger the aging of AlLi phase [30]. As a result, more and more AlLi particles precipitated from the β-Li matrix. These two regions were thus denoted as HAZ-solution and HAZ-aging, respectively. Generally, the microstructure in the FZ got coarsened with increasing laser power under 3.0 kW.

The Vickers hardness values in Fig. 8(a) showed a decreasing trend with increasing distance from the FZ. The hardness in the FZ was the highest among all the regions and was higher than that of the FZ of the as-cast plates because of the forging process. As the measurement points got away from the FZ, the hardness started to go down. When the distance was far enough, the hardness was stably low and was even lower than that of the as-forged base metal (HV 59.33, indicated by the cyan horizontal line). This is due to the softening effect of the AlLi precipitation [30]. The decreasing trend of hardness in the HAZ-solution is due to the softening effect of AlLi overcoming the solid solution strengthening effect, and the softening effect was more and more pronounced with a larger distance from the FZ. Recent studies on the precipitation phase have shown that the particles precipitated during the aging process are complicated, including MgLiZn phase [27], $(Mg,Li)_3Zn$ phase [28] or even Mg_3Al nanoparticles [31].

The tensile curves and mechanical properties are summarized in Figs. 8(b, c). Compared with the as-cast alloy, the as-forged alloy exhibited an increase of more than 20 MPa in both UTS and YS, with only a minor decrease in EL. Among all the LBW conditions, the optimal combination of the properties was obtained with the power of 2.1 kW/2.0 kW welding on double sides. Under this condition, the UTS was 184 MPa, the YS was 146 MPa and the EL was 10%.

3.3 Effect of solid solution on microstructure and tensile properties of welding joints

As can be seen from Fig. 9, the microstructure difference among the FZ, HAZ and BM was still apparent after solid solution treatment. The grain growth within the FZ was very slight while the grains in the HAZ and BM remained the same size. The main difference after solid solution can be seen from the SEM images in Fig. 10. The larger faceted Al_2Y phase was still present while the much smaller white AlLi particles were dissolved into the matrix,

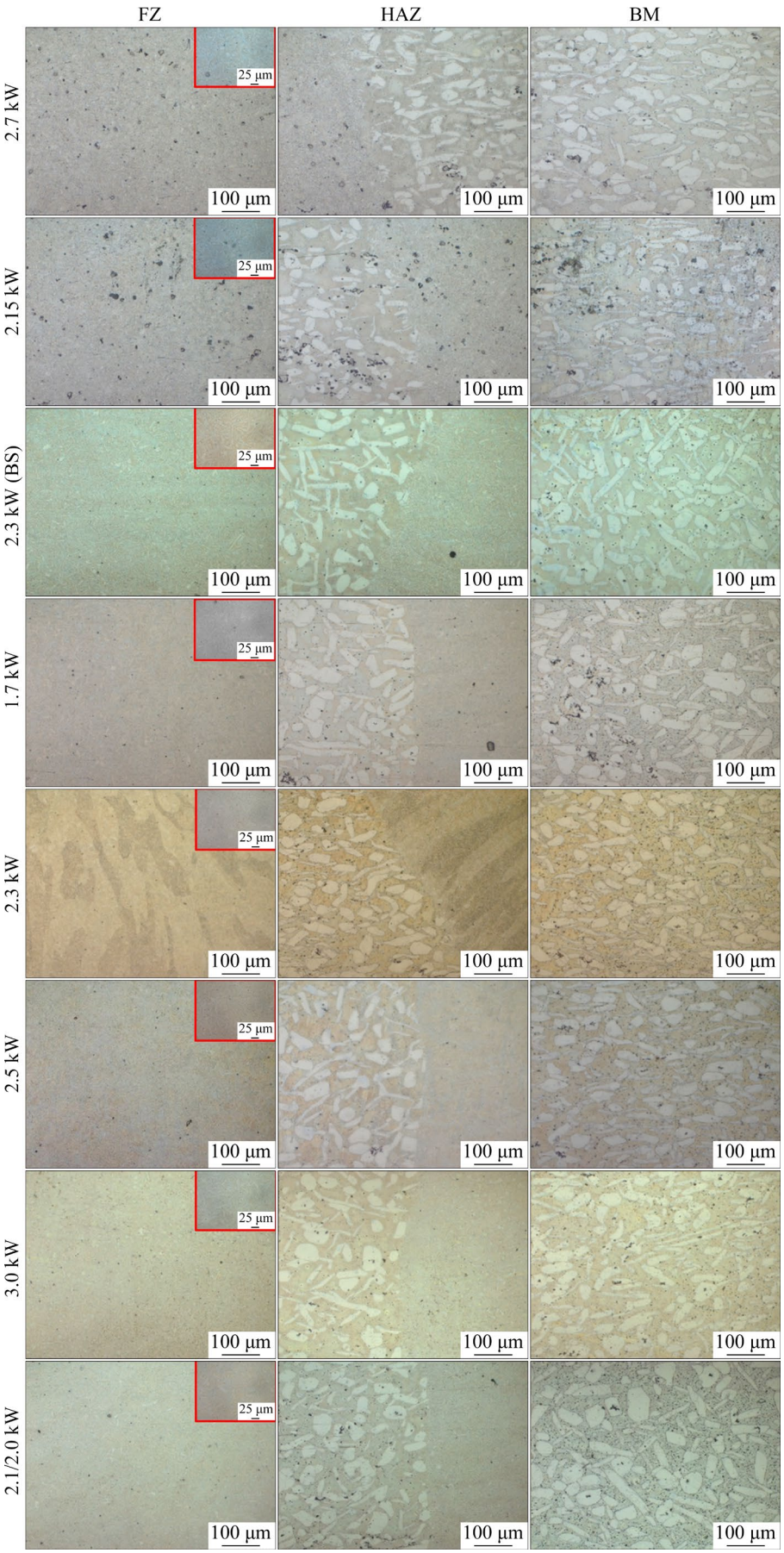

Fig. 6 OM images of FZ, HAZ and BM of LBW welding joints at various laser powers

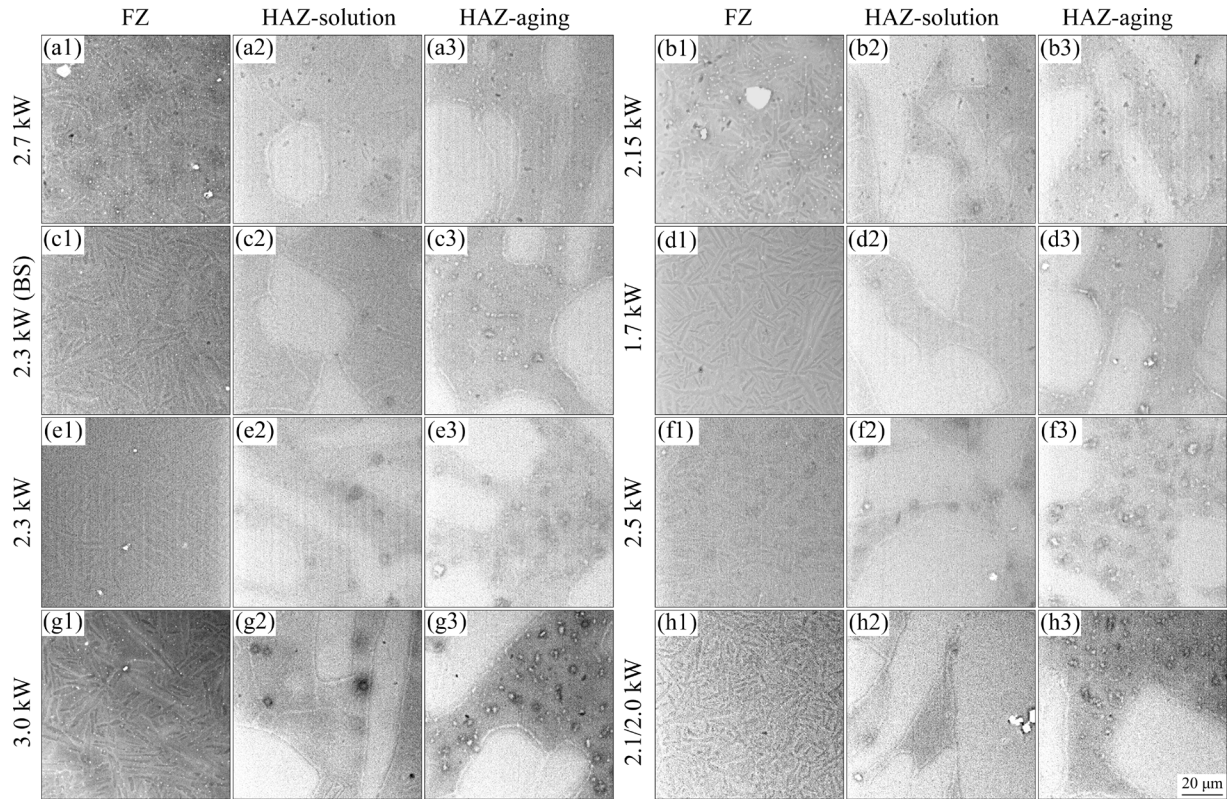

Fig. 7 SEM images of FZ, HAZ-solution and HAZ-aging of LBW welding joints at various laser powers

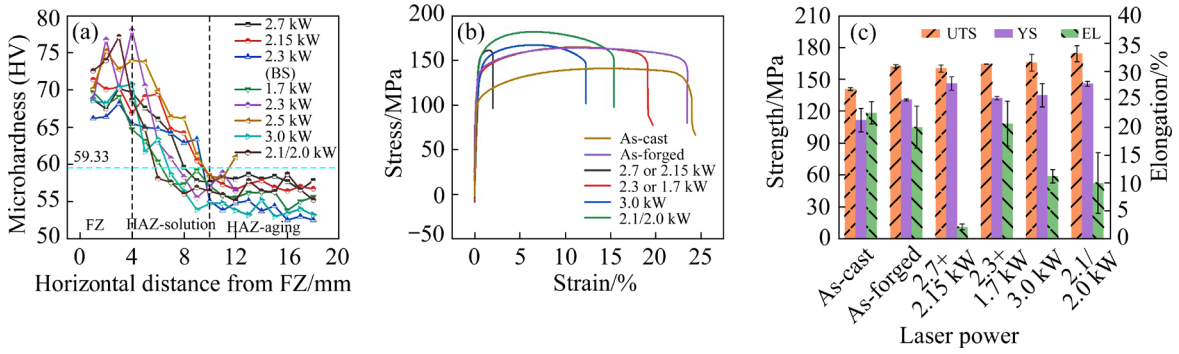

Fig. 8 Microhardness (a), tensile curves (b), and UTS, YS and EL (c) of LBW welding joints at different laser powers (Vickers hardness of as-forged alloy is indicated by cyan horizontal line in (a))

leading to the strengthening of the material. Clusters of Al_2Y can be observed in the HAZ and BM after solid solution, while the Al_2Y in the FZ was more uniformly distributed.

The Vickers hardness values of the TIG welding joints after solid solution treatment at 350 °C for 4 h are shown in Fig. 11(a). The cyan horizontal line indicated the hardness value of the as-cast alloy after the same solid solution treatment. It is thus clearly seen that the hardness of the welding joint at a current of 120 A was the highest and was even higher than that of the solid solution treated as-cast alloy. In addition, the hardness in the FZ of the 120 A welding joint was higher than that in the HAZ. The tensile curves of the welding joints at various currents after the solid solution, as well as the solid solution treated as-cast alloy were plotted in Fig. 11(b). The mechanical properties were summarized in Fig. 11(c). Generally, the mechanical properties of the welding joints after solid solution treatment were worse than those of the solid solution treated as-cast alloy. Among all the welding joints after solid solution treatment, the one at a current of 120 A showed the best mechanical properties (UTS: 217 MPa; YS: 188 MPa; EL: 6%).

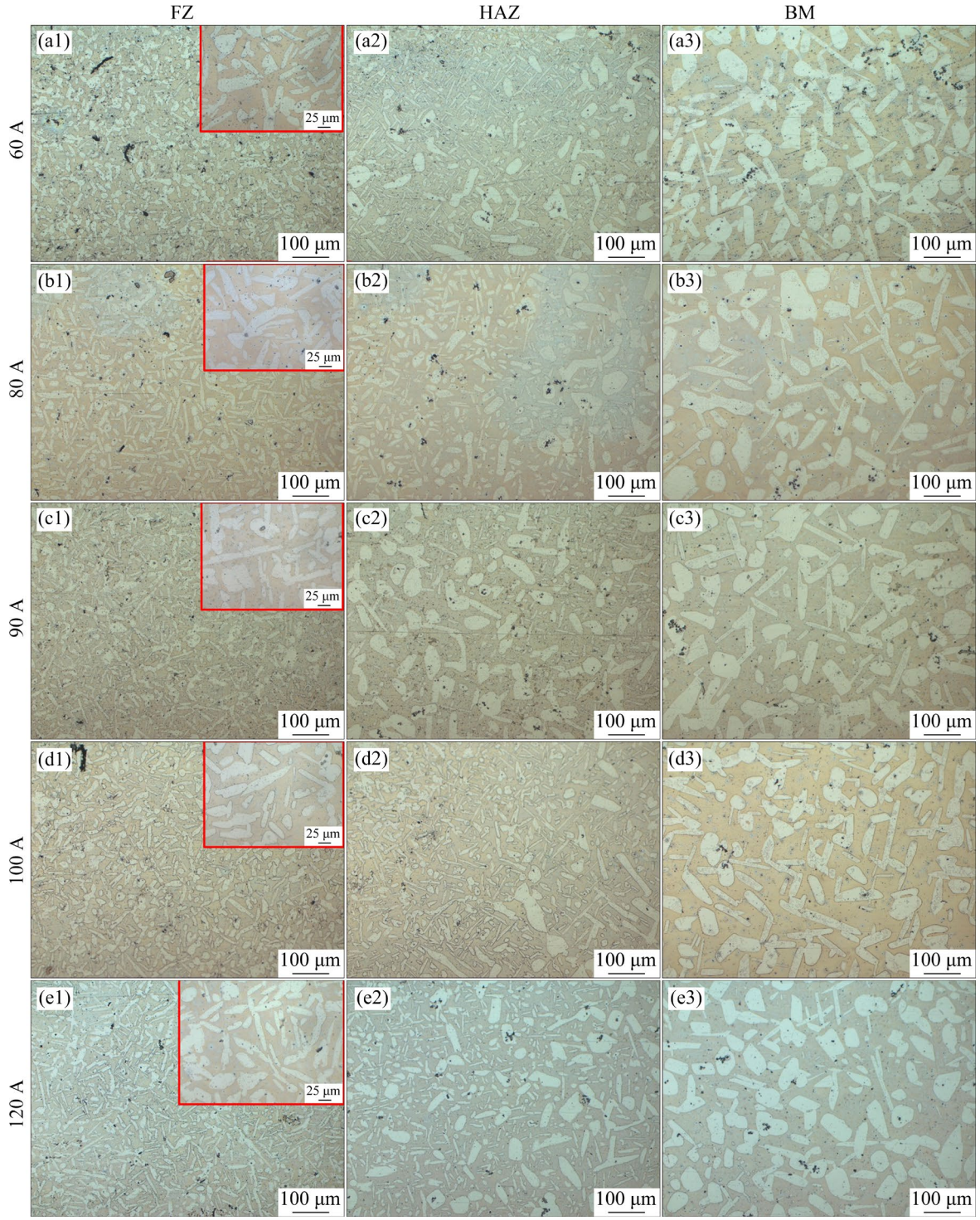

Fig. 9 OM images of FZ, HAZ and BM of TIG welding joints at various welding currents after solid solution treatment at 350 °C for 4 h

Like the microstructure of the LBW welding joints before solid solution treatment in Fig. 6, the boundaries between the FZ and HAZ in LBW welding joints were still apparent in Fig. 12. The α-Mg grains grew a little bit in the FZ due to the heat treatment but were still much finer than those in the BM. The α-Mg grains in the HAZ became less elongated and more globular, compared with the as-forged microstructure.

As can be seen in Fig. 13(a), the Vickers hardness of the LBW welding joints at the powers of 3 kW and 2.1/2.0 kW after solid solution

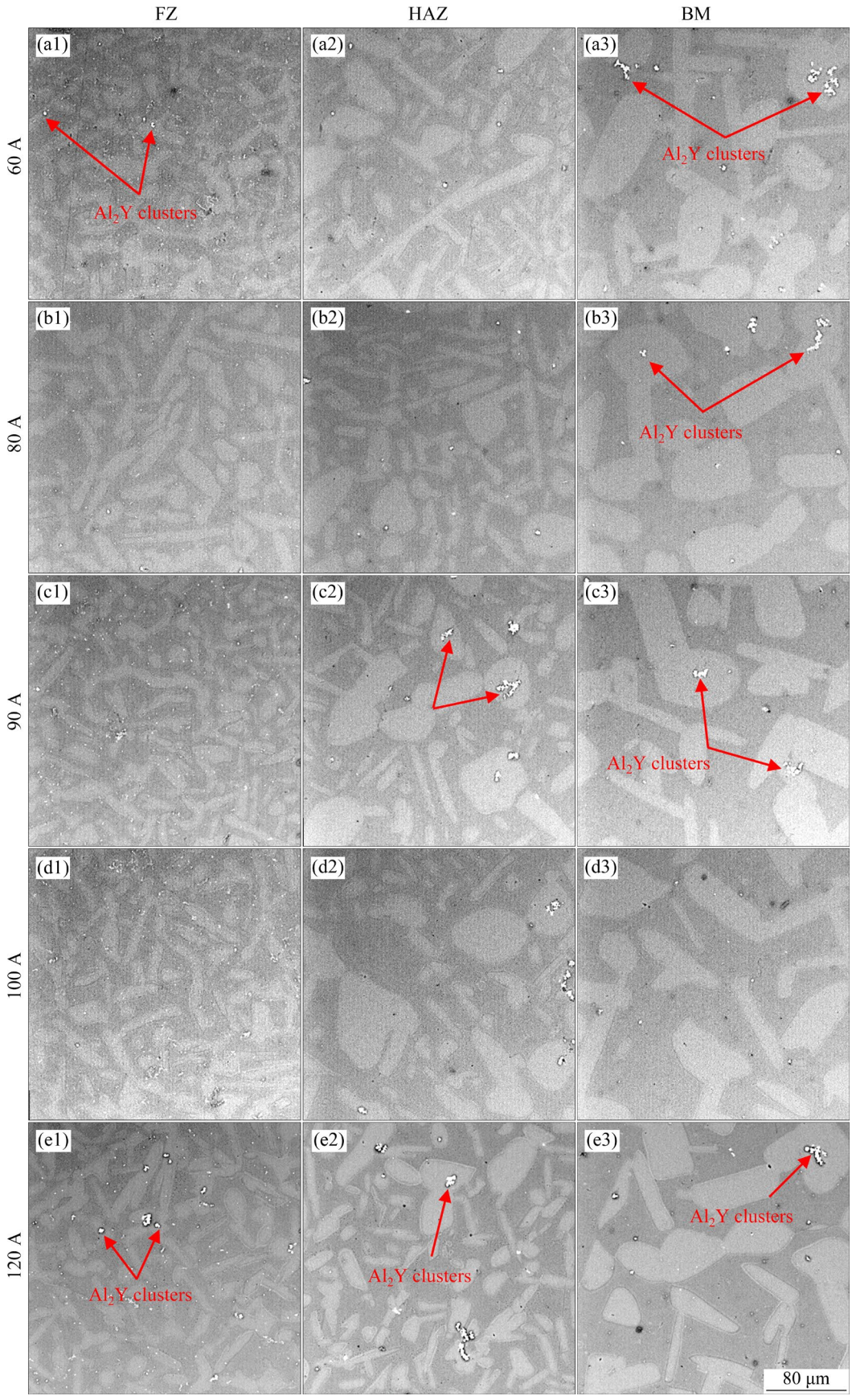

Fig. 10 SEM images of FZ, HAZ and BM of TIG welding joints at various welding currents after solid solution treatment at 350 °C for 4 h

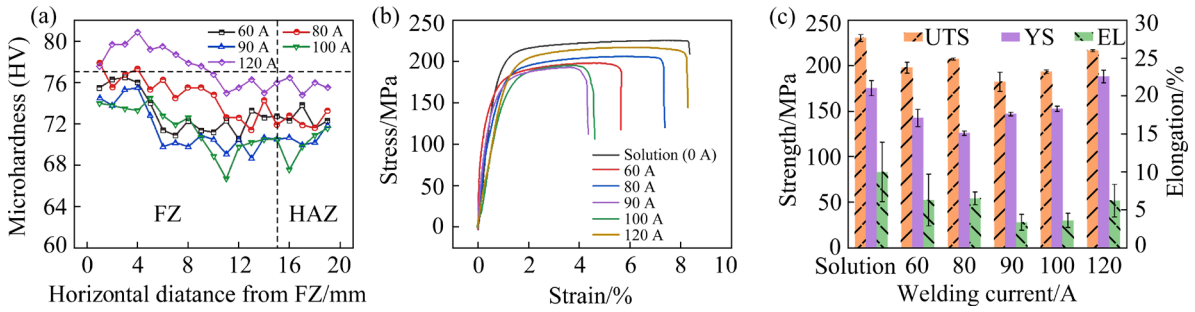

Fig. 11 Microhardness values (a), tensile curves (b), and UTS, YS and EL (c) of TIG welding joints after solid solution treatment at 350 °C for 4 h (Vickers hardness of as-cast alloy after the same solid solution treatment is indicated by the cyan horizontal line in (a))

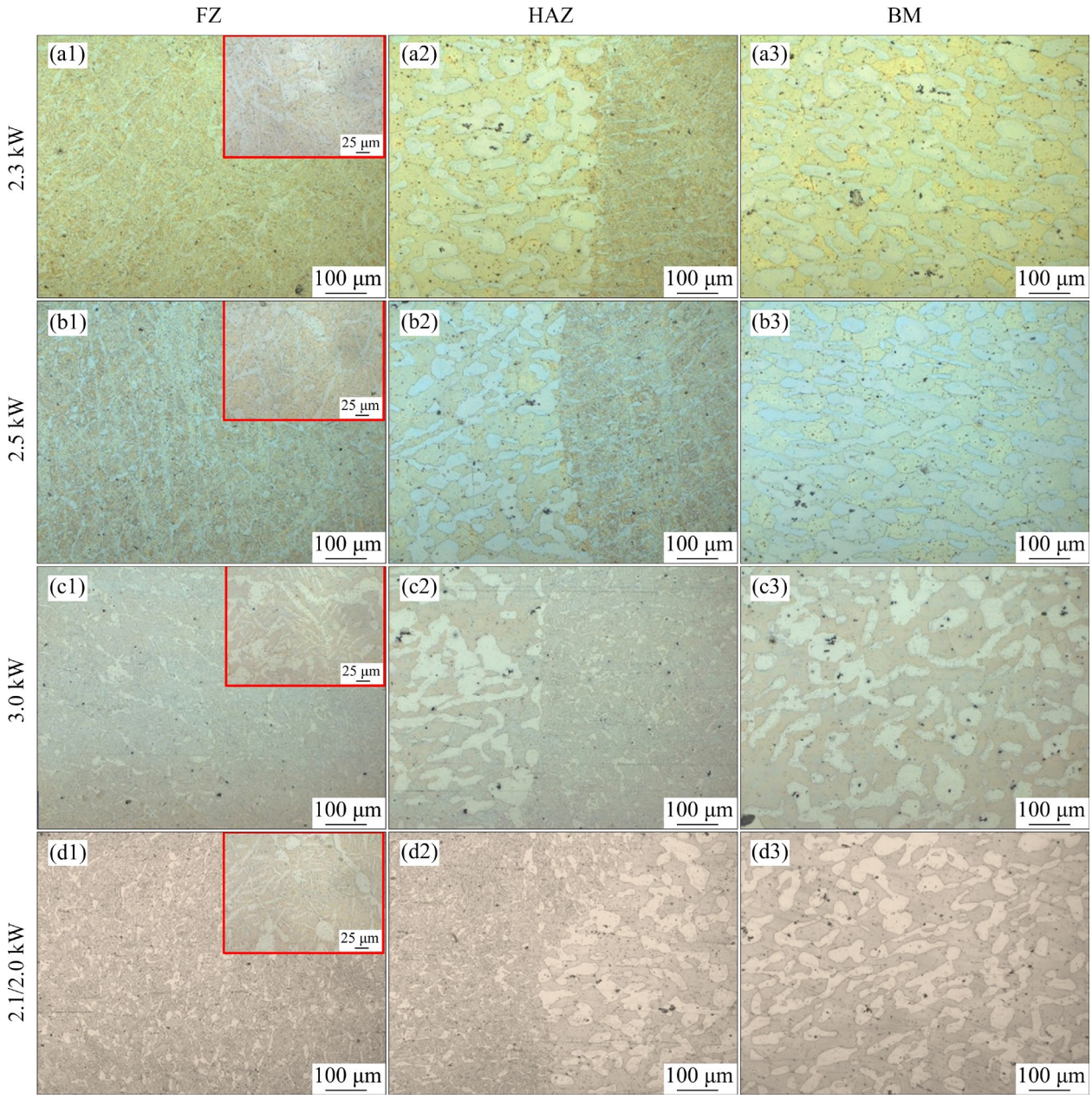

Fig. 12 OM images of FZ, HAZ and BM of LBW welding joints at various welding currents after solid solution treatment at 350 °C for 4 h

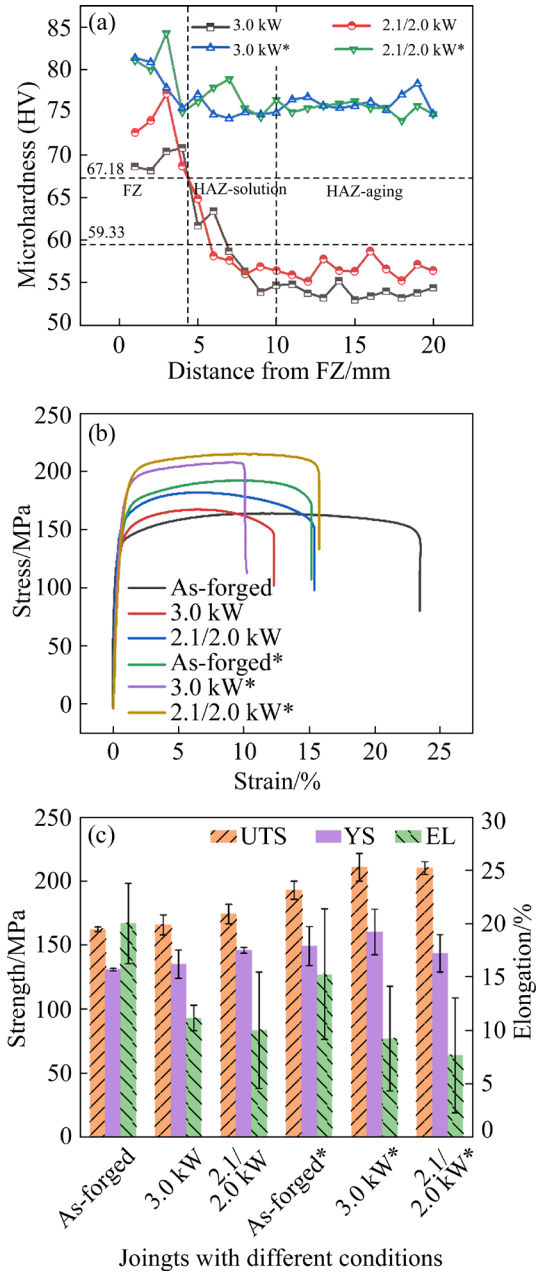

Fig. 13 Microhardness (a), tensile curves (b), and UTS, YS and EL (c) of LBW welding joints before and after (*) solid solution treatment at 350 °C for 4 h (Vickers hardness values of the as-forged alloy before (cyan line) and after (brown line) solid solution treatment are indicated in (a))

treatment (blue and green lines) increased significantly, especially in the HAZ. In addition, the hardness values were much higher than those of the solid solution treated as-forged alloy (brown line). From Figs. 13(b, c), the welding joint with the power of 3 kW showed the best combined properties after solid solution treatment (UTS: 211 MPa; YS: 160 MPa; EL: 9%).

3.4 Comparison of TIG and LBW techniques

TIG welding has been widely used in industry because of its low cost and high flexibility [32]. LBW welding is a welding approach with high energy density, high accuracy and high efficiency [20,32]. ZHANG et al [32] compared the laser and TIG welding of steels. The results showed that the width of the FZ by laser welding was 1.88 mm while the width of the LZ by TIG was 5.29 mm. In contrast, even though the depth of the FZ by laser welding (1.56 mm) was slightly smaller than that by TIG welding (2.01 mm), the shape of the FZ by laser welding below the surface was much smaller than that by TIG welding. The laser welding seemed to have better potential in Mg−Li alloy welding.

WU et al [23] investigated the wire-filled tungsten argon arc welding of Mg−14Li−1Al (LA141) alloy. The UTS of the LA141 plates after welding was 153 MPa, which was 95% that of the base metal and the EL remained ~8%. The HAZ in the welding seam was wide and the burning loss of Li was 23.6% under the argon protection. ZHANG et al [20] investigated the microstructure and mechanical properties of the Mg−10Li−3Al−3Zn laser welded joints. The width of the FZ was only ~0.8 mm and the microhardness of the FZ (HV 80−85) was much higher compared to those of the HAZ and BM (HV 65). The UTS of 166.8 MPa was obtained on the welded joint, which was almost the same as that of the base metal. In the present study, the UTS and YS of the welded joints using TIG and LBW exceeded those of the base metals (as-cast and as-forged alloys, respectively), which were better than the results in the above investigations.

4 Conclusions

(1) Among the welding currents of 60, 80, 90, 100, and 120 A, the TIG welding joint at a current of 80 A exhibited the best combination of mechanical properties: UTS of 159 MPa, YS of 122 MPa, and EL of 23%, exceeding the properties the as-cast alloy.

(2) Under the LBW conditions, the optimal combination of the properties was obtained with the power of 2.1 kW/2.0 kW double-side welding. Under this condition, the UTS was 184 MPa, the

YS was 146 MPa, and the EL was 10%, which were much higher than those of the TIG welding joints.

(3) After the solid solution treatment at 350 °C for 4 h, the change of α-Mg grains in the FZ, HAZ and BM of both the TIG and LBW welding joints was minor. In contrast, the larger faceted Al_2Y phase was still present while the much smaller white AlLi particles were dissolved into the matrix, leading to the strengthening of the welding joints. The UTS and YS of the TIG welding joint after solid solution treatment were 216 and 188 MPa, respectively, and were both better than those of the LBW welding joint (211 and 160 MPa, respectively).

CRediT authorship contribution statement

Jia-wei LU: Conceptualization, Investigation, Methodology, Formal analysis, Data curation, Writing − Original draft; **Hong-jie LIU:** Conceptualization, Investigation, Methodology, Formal analysis, Data curation, Writing − Original draft; **Lian-mei WU:** Writing − Review & editing; **Jia-xin YU:** Data curation, Writing − Review & editing; **Yu-chuan HUANG:** Data curation, Writing − Review & editing; **Jia-wei SUN:** Writing − Review & editing; **Guo-hua WU:** Writing − Review & editing, Supervision; **Wen-xia HU:** Writing − Review & editing; **Fei LI:** Writing − Review & editing; **Jun-feng LI:** Writing − Review & editing; **Wen-cai LIU:** Supervision, Funding acquisition, Conceptualization, Writing − Review & editing.

Declaration of competing interest

The authors declare that they have no known competing financial interests or personal relationships that could have appeared to influence the work reported in this paper.

Acknowledgments

This study was financially supported by the National Defense Basic Research Program of China (No. JCKY2023204A005), the Research Program of Joint Research Center of Advanced Spaceflight Technologies of China (No. USCAST2023-3), the National Natural Science Foundation of China (No. U2037601), the Major Scientific and Technological Innovation Project of Luoyang, Henan Province, China (No. 2201029A), and the Foundation Strengthening Plan Technical Field Fund, China (No. 2021-JJ-0112).

References

[1] HUNG Sung-mao, LIN Han, CHEN Huan-wen, CHEN Siao-ying, LIN Chao-sung. Corrosion resistance and electrical contact resistance of a thin permanganate conversion coating on dual-phase LZ91 Mg−Li alloy [J]. Journal of Materials Research and Technology, 2021, 11: 1953−1968.

[2] HUANG Yu-chuan, ZHANG Quan-da, OUYANG Si-jie, SUN Fu-zhen, SUN Jia-wei, LI Hui-yu, WU Guo-hua, CHEN Pei-jun, LIU Wen-cai. Effects of Zn and Gd contents and their ratios on microstructure and mechanical properties of as-cast and as-extruded Mg−8Li alloys [J]. Transactions of Nonferrous Metals Society of China, 2024, 34: 798−811.

[3] PENG Xiang, SUN Jia-wei, LIU Hong-jie, WU Guo-hua, LIU Wen-cai. Microstructure and corrosion behavior of as-homogenized and as-extruded Mg−xLi−3Al−2Zn−0.5Y alloys (x=4, 8, 12) [J]. Transactions of Nonferrous Metals Society of China, 2022, 32: 134−146.

[4] PENG Xiang, LIU Wen-cai, WU Guo-hua. Effects of Li content on microstructure and mechanical properties of as-cast Mg−xLi−3Al−2Zn−0.5Y alloys [J]. Transactions of Nonferrous Metals Society of China, 2022, 32: 838−849.

[5] PENG Xiang, LIU Wen-cai, WU Guo-hua, JI Hao, DING Wen-jiang. Plastic deformation and heat treatment of Mg−Li alloys: A review [J]. Journal of Materials Science & Technology, 2022, 99: 193−206.

[6] ZHAO Jiong, ZHANG Jie, LIU Wen-cai, WU Guo-hua, ZHANG Liang. Effect of Y content on microstructure and mechanical properties of as-cast Mg−8Li−3Al−2Zn alloy with duplex structure [J]. Materials Science and Engineering: A, 2016, 650: 240−247.

[7] ZHAO Jiong, LI Zhong-quan, LIU Wen-cai, ZHANG Jie, ZHANG Liang, TIAN Ying. Influence of heat treatment on microstructure and mechanical properties of as-cast Mg−8Li−3Al−2Zn−xY alloy with duplex structure [J]. Materials Science and Engineering: A, 2016, 669: 87−94.

[8] JI Hao, PENG Xiang, ZHANG Xiao-long, LIU Wen-cai, WU Guo-hua, ZHANG Liang, DING Wen-jiang. Balance of mechanical properties of Mg−8Li−3Al−2Zn−0.5Y alloy by solution and low-temperature aging treatment [J]. Journal of Alloys and Compounds, 2019, 791: 655−664.

[9] ZOU Yun, ZHANG Le-hao, LI Yang, WANG Hong-tao, LIU Jia-bin, LIAW P, BEI Hong-bin, ZHANG Zhong-wu. Improvement of mechanical behaviors of a superlight Mg−Li base alloy by duplex phases and fine precipitates [J]. Journal of Alloys and Compounds, 2018, 735: 2625−2633.

[10] PENG Xiang, LIANG Xin-li, LIU Wen-cai, WU Guo-hua, JI Hao, TONG Xin, ZHANG Liang. High-cycle fatigue behavior of Mg−8Li−3Al−2Zn−0.5Y alloy under different states [J]. Journal of Magnesium and Alloys, 2021, 9: 1609−1618.

[11] GUO Fei, JIANG Lu-yao, MA Yan-long, LIU Lei, ZHANG Zhen, YANG Ming-bo, ZHANG Ding-fei, PAN Fu-sheng. Strengthening a dual-phase Mg–Li alloy by strain-induced phase transformation at room temperature [J]. Scripta Materialia, 2020, 179: 16−19.

[12] LIAO Guang-lan, WU Guo-hua, LIU Wen-cai, SUN Jia-wei, LV Xiao, PANG Song, CHEN Pei-jun. Microstructure evolution and enhanced fatigue behavior in the

Mg−10Li−5Zn−0.5Er alloys micro-alloyed with Yb [J]. Journal of Magnesium and Alloys, 2024, 12: 3159−3172.

[13] LIU Hong-jie, MA Jia, LIU Wen-cai, WU Guo-hua, SUN Jia-wei, TONG Xin, CHEN Pei-jun. Influence of TIG welding process parameters on microstructure and mechanical properties of as-cast Mg−8Li−3Al−2Zn−0.5Y alloy [J]. Journal of Materials Research and Technology, 2022, 20: 4114−4129.

[14] GAN Yi, HU Li, SHI Lai-xin, CHEN Qiang, LI Ming-ao, XIANG Lin, ZHOU Tao. Effect of AlLi phase on deformation behavior and dynamic recrystallization of Mg−Li alloy during hot compression [J]. Transactions of Nonferrous Metals Society of China, 2023, 33: 1373−1384.

[15] GAO Shi-kang, ZHAO Hong-yun, LI Gao-hui, MA Ling-hang, ZHOU Lo, ZENG Ru-chuan, LI Dong-xiao. Microstructure, properties and natural ageing behavior of friction stir welded dual-phase Mg−Li alloy [J]. Journal of Materials Processing Technology, 2024, 324: 118252.

[16] ZHU Yi-xing, ZHOU Meng-ran, GENG Ying-xin, ZHANG Shun, XIN Tong-zheng, CHEN Gao-qiang, ZHOU Yi-fan, ZHOU Xiao-yu, WU Rui-zhi, SHI Qing-yu. Microstructural evolution and its influence on mechanical and corrosion behaviors in a high-Al/Zn containing duplex Mg−Li alloy after friction stir processing [J]. Journal of Materials Science and Technology, 2024, 184: 245−255.

[17] ZHANG Zi-yan, CHEN Kang-hua, NI Er-fu, Effect of magnesium on the electrochemical behavior of lithium anode in LiOH aqueous solution used for lithium−water battery [J]. Electrochimica Acta, 2010, 55: 3830−3837.

[18] LIU Zhan, NIE Jin-feng, ZHAO Yong-hao. Effect of deformation processing on microstructure evolution and mechanical properties of Mg−Li alloys: A review [J]. Transactions of Nonferrous Metals Society of China, 2024, 34: 1−25.

[19] ZHOU M R, MORISADA Y, FUJII H, WANG J Y. Microstructure and mechanical properties of friction stir welded duplex Mg−Li alloy LZ91 [J]. Materials Science and Engineering: A, 2020, 773: 138730.

[20] ZHANG Lin-jie, ZHANG Hai-bo, LEI Xiao-wei, WANG Rui, HAN Bai-feng, ZHANG Jian-xun, NA S J. Laser processing of Mg−10Li−3Al−3Zn alloy: Part I. Microstructure and properties of laser welded joints [J]. Journal of Manufacturing Processes, 2020, 57: 871−880.

[21] LIU Yu-qiang, YU De-shui, ZHANG Yan, ZHOU Jian-ping, SUN Da-qian, LI Hong-mei. Research advances on weldability of Mg alloy and other metals worldwide in recent 20 years [J]. Journal of Materials Research and Technology, 2023, 25: 3458−3481.

[22] LIU Xu-he, GU Shi-hai, WU Rui-zhi, LENG Xue-song, YAN Jiu-chun, ZHANG Mi-lin. Microstructure and mechanical properties of Mg−Li alloy after TIG welding [J]. Transactions of Nonferrous Metals Society of China, 2011, 21: 477−481.

[23] WU Guo-qing, ZHAO Deng-chuan, SUN Lu-bo, Microstructure and mechanical properties of wire-filled tungsten argon arc welded joints for LA141 magnesium−lithium−aluminum alloy [J]. Materials Today Communications, 2020, 23: 100881.

[24] EVANS S, WANG Jie, QIN Jian, HE Yong-peng, SHEPHERD P, DING Jia-luo. A review of WAAM for steel construction—Manufacturing, material and geometric properties, design, and future directions [J]. Structures, 2022, 44: 1506−1522.

[25] LIN Zi-dong, SONG Kai-jie, YU Xing-hua. A review on wire and arc additive manufacturing of titanium alloy [J]. Journal of Manufacturing Processes, 2021, 70: 24−45.

[26] WANG Lei-lei, XUE Jia-xiang, WANG Qiang. Correlation between arc mode, microstructure, and mechanical properties during wire arc additive manufacturing of 316L stainless steel [J]. Materials Science and Engineering: A, 2019, 751: 183−190.

[27] HUANG Yu-chuan, QI Fang-zhou, SUN Jia-wei, XU Yang-yang, GUO You-jie, YU Jia-xin, YI Ling-fan, TAO Xin-miao, WU Guo-hua, LIU Wen-cai. Strengthening dual-phase Mg−Li alloy through precipitation control [J]. Materials Research Letters, 2025, 13: 17−23.

[28] JI Hao, WU Guo-hua, LIU Wen-cai, ZHANG Xiao-long, ZHANG Liang, WANG Ming-wu. Origin of the age-hardening and age-softening response in Mg−Li−Zn based alloys [J]. Acta Materialia, 2022, 226: 117673.

[29] AL-SAMMAN T. Comparative study of the deformation behavior of hexagonal magnesium−lithium alloys and a conventional magnesium AZ31 alloy [J]. Acta Materialia, 2009, 57: 2229−2242.

[30] ALAMO A, BANCHIK A D. Precipitation phenomena in the Mg−31at.%Li−1at.%Al alloy [J]. Journal of Materials Science, 1980, 15: 222−229.

[31] TANG Song, XIN Tong-zheng, XU San-qiang, MISKOVIC D, SHA Gang, QUADIR Z, RINGER S, NOMOTO K, BIRBILIS N, FERRY M. Precipitation strengthening in an ultralight magnesium alloy [J]. Nature Communications, 2019, 10: 1003.

[32] ZHANG Yan-song, WANG Hong-ze, CHEN Kun-kun, LI Shu-hui. Comparison of laser and TIG welding of laminated electrical steels [J]. Journal of Materials Processing Technology, 2017, 247: 55−63.

TIG 和 LBW 焊接 Mg−8Li−3Al−2Zn−0.5Y 合金的显微组织与力学性能

陆嘉伟[1]，刘宏杰[1]，武练梅[2]，于佳新[1]，黄玉川[1]，
孙家伟[1]，吴国华[1]，胡雯霞[2]，李 霏[2]，李俊峰[3]，刘文才[1]

1. 上海交通大学 材料科学与工程学院 轻合金精密成型国家工程研究中心和金属基复合材料全国重点实验室，上海 200240；
2. 北京电子工程总体研究所，北京 100854；
3. 上海云铸三维科技有限公司，上海 201306

摘 要：对铸态和锻造态 Mg−8Li−3Al−2Zn−0.5Y(LAZ832-0.5Y)合金进行钨极惰性气体焊接(TIG)和激光束焊接(LBW)以探索合金的可焊性。为了进一步提高焊后接头的强度，在 350 ℃时，对合金进行 4 h 固溶处理，并进行了显微组织表征和力学性能测试。当 TIG 的焊接电流为 80 A 时，最佳铸态焊接接头的极限抗拉强度(UTS)和屈服强度(YS)分别为 159 和 122 MPa，比 LBW 的最佳焊接接头(2.1 kW/2.0 kW 双面焊接)的 UTS(184 MPa)和 YS (146 MPa)低。经固溶处理后，一方面，在两种焊接接头的熔融区(FZ)、热影响区(HAZ)和基体材料区(BM)的显微组织中，α-Mg 晶粒长大不明显；另一方面，较大的 Al_2Y 相在固溶处理后仍然存在，而较小的白色 AlLi 相在固溶处理后完全溶入基体，产生了固溶强化。经固溶处理后 TIG 焊接接头的 UTS 和 YS 分别增加到 216 和 188 MPa，而 LBW 焊接接头的 UTS 和 YS 仅分别增加到 211 和 160 MPa。

关键词：镁锂合金；钨极惰性气体焊接；激光束焊接；显微组织；力学性能；热处理

(Edited by Wei-ping CHEN)